Sādhanā (2023)48:224
https://doi.org/10.1007/s12046-023-02298-7

Numerical and experimental studies on feasibility of a cryogenic turboexpander rotor supported on gas foil bearings

DEBANSHU S KHAMARI* and SURAJ K BEHERA

National Institute of Technology, Rourkela, Sundergarh, Odisha 769008, India
e-mail: debanshushekhar@gmail.com

MS received 25 November 2022; revised 6 February 2023; accepted 13 August 2023

Abstract. Gas foil bearings are gaining popularity for their compliance properties in various high-speed turbomachinery applications such as air cycle machine, turbocompressor, turbocharger, turboexpander etc. A modest attempt is made in the current research to study the feasibility of gas foil bearing for a turboexpander rotating at 1,75,000 rpm. The turboexpander rotor with 16 mm diameter and 91 mm length used for experimentation is supported by a pair of gas foil journal bearings and mounted with turbine and compressor wheels at both ends of the rotor. The feasibility study was performed based on comparison of rotodynamic analysis and experimental data for the critical speed of the rotor and unbalance response at bearing locations. The critical speeds and the unbalance response are predicted using the finite element analysis, which takes into account the gyroscopic effect, shear deformation, internal damping, inertia of the rotor and the dynamic coefficients of the gas foil bearing. The predicted and experimental variation of critical speed is found to be within a relative error of 3–6%; similarly, the variation of unbalance response was found with a relative error of 2–9%. The low relative errors suggest that the experiment and prediction methodology are credible. The author believes that the rotodynamic analysis methodology will be quite valuable for researchers working in the area of high-speed rotors supported with gas foil bearings.

Keywords. Turboexpander; rotordynamics; high-speed rotor; gas foil bearing.

1. Introduction

Compact-sized turbomachinery rotates at high speed and is supported with oil free bearings. Gas foil bearing is one of the appropriate candidate for such turbomachinery due to its compliant behavior and higher load-carrying capacity compared to conventional gas bearings [1]. Also, various factors, such as gyroscopic effect, shear deformation, axial torque, internal friction, viscous damping and bearing forces, cannot be ignored for a flexible rotor as these influence their rotordynamic behavior. They collectively respond to critical speed, synchronous whirl, instability, and other factors. Therefore, the feasibility study of high-speed rotors supported with gas foil bearings is one of the focus areas among researchers around the world.

In the current scenario, the design of turbomachinery is majorly focused on obtaining high speed with improved reliability and efficiency [2]. Aerodynamic journal bearings (AJBs) are particularly valuable when they support high-speed rotors that are preferably lightly loaded [3]. Researchers have explored the static and dynamic characteristics of AJBs in the past. The effect of gas rarefication [4, 5] and slip flow [6] on the performance of the AJBs have been incorporated. Recently, new designs have been suggested in order to improve the performance of these bearings. Pattnayak *et al* [7] proposed a new design for an AJB that incorporated both bump foil and rigid sector segments. It is observed that the new bore design significantly improved the load-carrying capacity and dynamic stability compared to traditional bump foil bearings. Subsequently, Pattnayak *et al* [8] developed an AJB with a combination of pockets and textures on the bore. This design resulted in a 3–21% increase in the minimum film thickness, a 3–12% decrease in the coefficient of friction, and a 3–12% reduction in the friction force compared to traditional journal bearing. Other than pockets, textures and bores, modifications of the journal by providing herringbone grooves on the surface have been readily used [9–11]. The grooved design along with the optimization has led to a 25% reduction in windage losses and a 35% improvement in the stability margin of AJBs [12]. A state-of-the-art review related to the performance behaviors of the AJBs has been presented [13]. Notably, foil journal bearings outperform rigid bearings, but there is still room for development in terms of their load-carrying capability and stability. The use of foil bearing enables the turbomachinery to achieve high speed and operate in an oil-free environment. In the 1990s, gas foil bearings were first designed

*For correspondence
Published online: 21 October 2023

for small-sized high-speed rotors [14, 15]. It was observed that adequate clearance, bearing stiffness and damping enable the rotor to achieve sufficient operational performance. Subsequently, foil journal bearings were used in a cryogenic turboexpander for high speed application up to 230,000 rpm [16]. Foil bearings were found to have high stability during operations. It was observed that a feasibility study needs to be conducted to test the turboexpander for stable operation of the cryogenic system. Hou *et al* conducted a feasibility study of a turboexpander rotor supported on a 25 mm diameter plate foil bearing [17]. It was observed that the foil bearings provide higher system stability and performance compared to rigid bearings. After that, a cryogenic turboexpander was successfully tested up to a speed of 100,000 rpm both in vertical and horizontal setups [18]. The rotor was tested, and an abysmal difference was observed in the performance with horizontal and vertical orientation. The experiments further validated the suitability of gas foil bearings for oil-free turbomachinery. After that, the performance of two different types of gas foil bearings was experimentally investigated for a cryogenic turboexpander at a speed of 220,000 rpm [19]. It was found that both the gas foil bearings had improved rotor dynamic capabilities, making them more suitable for high-speed applications. Later, a turboexpander rotor was tested up to a speed of 100,000 rpm, which was supported on multi-decked protuberant gas foil bearings [20]. The support stiffness was altered by varying the thickness of the protuberant foils. It was observed that the rotor vibration amplitude decreases with the increase in support stiffness. The decrease in the radial clearance, on the other hand, resulted in a lower rotational speed of the turboexpander. The unbalance response of the rotor was found to decrease with the increasing structural damping of the bearing, indicating that rotor stability is significantly influenced by the bearing damping [21].

Numerical study of the turboexpander requires precise consideration in dynamic modeling due to their compact configuration and complicated rotor-bearing system. There are three key aspects to consider while modeling the complicated rotor bearing system [22]. (i) Modeling the bearing while providing a reasonable clearance in mind to compute stiffness and damping. (ii) Representation of the disc, turbine, and compressor as a lumped mass and incorporate it in the motion equation. Finally, (iii) solving the globalized equation to investigate the system's viability and performance at very high speeds. So considering all the above stated factors, modeling the turboexpander system becomes complicated. The finite element (FE) method is one of the approaches, which enables such systems to extract most frequencies with fewer elements and computational time [23]. FE method helps to predict the eigen frequencies, mode shapes and critical speeds of the rotating system, which are essential for the safety of the entire system. These investigations are vital in avoiding the high level of vibrations and resonance conditions [24]. The dynamic analysis of a high-speed turboexpander is a relevant area of investigation as it depicts the rotor response characteristics as well as the bearing dynamic characteristics [25].

The literature review suggests that there is a wide array of methods available for increasing gas foil journal bearings performance; however, only a few studies have been published on the experimental feasibility study of gas foil bearing supported rotors. The lack of reliable experimental test data and accurate rotodynamic predictions has delayed the widespread usage of gas foil bearings in high-speed turbomachinery. In the present work, the rotordynamic analysis is conducted based on the finite element method. Further, a turboexpander rotor along with gas foil bearings is fabricated, tested, and the results are discussed. The feasibility of the gas foil bearings is studied by comparing the prediction of rotor vibration using FE analysis and experimental results.

2. Description of the turboexpander rotor and experimental facility

The rotor consists of an expansion turbine, a brake compressor and a shaft with a collar subsystem. The turbine wheel is situated at one end, whereas the compressor wheel is at the other end. The collar is located nearer to the brake compressor to control the dimension of the rotor and enable compactness and easier assembly of the turbomachinery. Steps are provided at both ends of the shaft for the seating of the turbine and compressor. This helps in locating the turbine and compressor in the radial direction. The step located some distance away from the turbine wheel decreases the cross-section of the shaft, lowering the heat transfer rate from the lower bearing region to the cold end. Figure 1 shows the configuration of the cryogenic turboexpander.

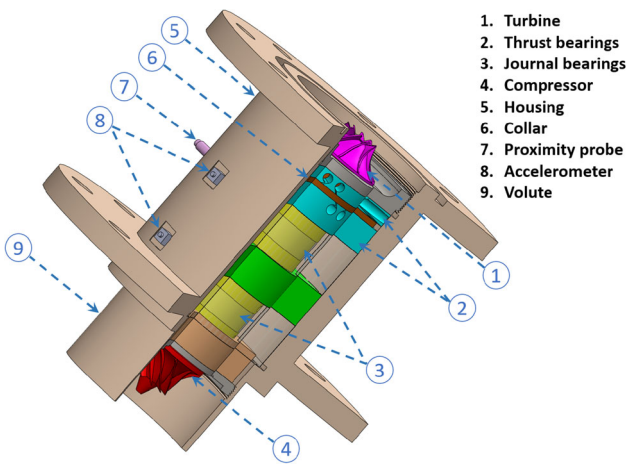

Figure 1. Configuration of the turboexpander.

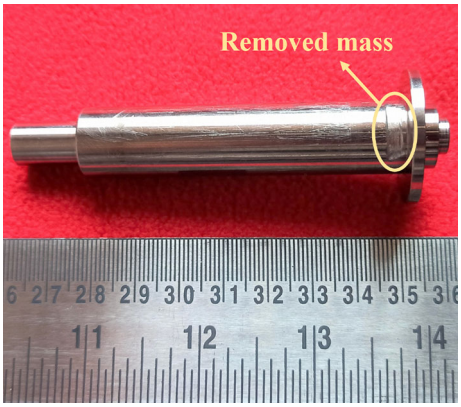

Figure 2. Balanced rotor with removed mass.

The fabricated rotor is balanced with 2.5G in order to avoid any unwanted vibratory response. The shaft along with turbine and compressor wheel attached at both ends was balanced using a precision balancing machine (Schenck Ro Tec GmBH make) with hard bearing. The planes for the removal of balancing mass are selected near the bearings. The residual unbalance in both the balancing planes are kept within 40 mg-mm. The rotor with removed mass after balancing is shown in figure 2. The parameters of the turboexpander rotor are given in table 1.

The turboexpander rotor is supported on gas foil bearings. Gas foil journal bearing (GFJB) has three parts: the housing, the top foil and the bump foil. The foils are inserted through the rectangular slot in the bearing housing and bent while carefully regulating the height of the foil in the attachment point. Both the top foil and bump foil are fixed to the housing using pins and grub screws. Phosphor bronze material is chosen for fabricating the foils due to its better friction properties, self-lubricating characteristics and suitability for low-temperature applications. The detailed parameters of the GFJB are given in table 2. Gas foil thrust bearing (GFTB) consists of similar parts to that of the journal bearing but different arrangements. The bearing base contains partial-arc slots to hold the foil components which are hinged at one edge. The slots are given at 90° at one another, dividing the bearing base into four pads. The thickness of the slots should be adequate to handle the realistic range of foil thicknesses, while yet allowing a tiny gap in the hinge to allow motion. The bump foil is first attached to the pads. The top foil is then positioned so that the leading edge of the top foil is aligned with the trailing edge of the bump foil. After inserting the foils in their corresponding slots, the pins and grub screws are utilized to keep the foils in place throughout the operation. Moreover, the top foil is covered with the solid lubricant MoS_2 to reduce wear on the top foil and collar of the rotor during the rotor start and stop. The detailed parameters of the GFTB are listed in table 3. Figure 3 shows all the components of the turboexpander.

The turboexpander is attached to a number of vibration measurement equipment such as NI (National Instruments) data acquisition system with a NI vibration card, oscilloscope, proximity probes, a digital tachometer and piezoelectric accelerometers. The turboexpander is a critical equipment that needs a compressed air facility to run in a dust-free environment and operate at high-speed conditions. Various components required for the safe operation of the turboexpander include a compressor, an air filter, an air purifier, a cooler, a reservoir, a plate-fin heat exchanger, and a test bench. A schematic diagram of the test setup highlighting all the parts is illustrated in figure 4. The compressed air facility consists of an air purifier unit, a filter, a moisture absorber, and a screw compressor (KAESER SIGMA BSD 72). To produce clean air, the filter has a three-layer filtering system that filters solid dust

Table 1. Geometrical parameters of the turboexpander rotor.

Parameter	Magnitude	Parameter	Magnitude
Diameter of turbine (mm)	15	Thickness of compressor (mm)	12
Thickness of turbine (mm)	10	Density of compressor (kg/m^3)	2700
Density of turbine (kg/m^3)	2700	Diameter of collar (mm)	28
Diameter of compressor (mm)	26	Thickness of collar (mm)	2.5

Table 2. Parameters of GFJB.

Parameter	Magnitude	Parameter	Magnitude
Length of bearing (mm)	16	Eccentricity ratio	0.8
The radius of the shaft (mm)	8	Bump length (mm)	2.64
Bump foil thickness (mm)	0.1	Speed of the shaft (rpm)	2,40,000
Pitch of bump (mm)	4.20	Viscosity of He (N-s/mm^2)	19.6×10^{-12}
Poisson's ratio	0.272	Young's modulus (GPa)	210

Table 3. Parameters of GFTB.

Parameter	Magnitude	Parameter	Magnitude
Inner radius of the bearing (mm)	8.06	Young's modulus	210
Outer radius of the bearing (mm)	37	Poison ratio	0.272
Min. film thickness (μm)	25	Speed of the shaft (rpm)	2,40,000
Bump foil thickness (mm)	0.1	Viscosity of He (N-s/mm^2)	19.6×10^{-12}
Bump foil pitch (mm)	4.2	Radius of the bump (mm)	1.75
Half-bump length (mm)	2.1	Angular extent of the pad (radian)	π/2

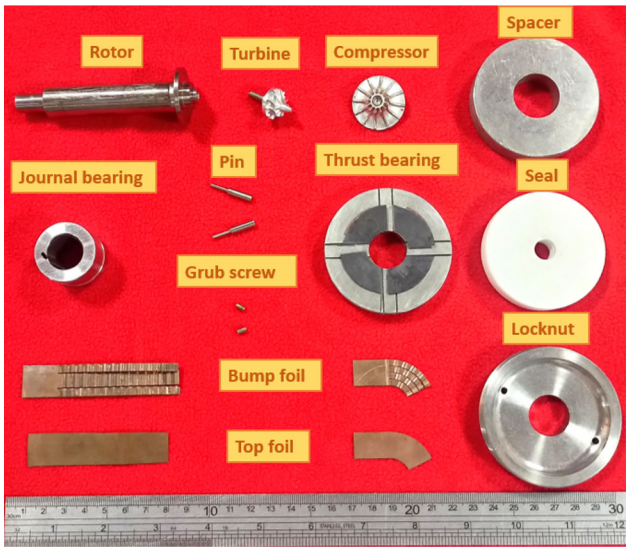

Figure 3. Components of the turboexpander.

particles, water particles, and oil particles. Clean air is directed via a Freon cooler to generate dry, subcooled, and dehumidifying air. The air is then kept at a certain pressure in a surge tank. After that, a plate-fin heat exchanger lowers the temperature of the air to make it appropriate for a turboexpander arrangement. Additionally, perlite powder and nitrile rubber polyethylene pipe are used to insulate the turbine supply line. Along with thermocol insulation sheet, perlite powder is also used to insulate the PFHX.

Figure 5 shows the experimental test setup, which includes all components such as a compressed air facility, a NI cDAQ-9185 (National Instruments compact data acquisition) system equipped with a four-channel NI 9234 vibration card, and various measurement equipment installed on the turboexpander housing. Two proximity probes, three piezoelectric accelerometers and a digital oscilloscope are utilized for vibration analysis. The proximity probes are the inductive type which are mounted on the bearing housing to measure the rotor displacement or vibration. The probe is threaded into the hole drilled on the bearing housing and secured at a short distance from the rotor. As the rotor rotates, the probe measures the movement, converting it to a proportional voltage that is monitored with the DAQ system. The two proximity probes are mounted on the housing at 90° to one another, which makes it possible to monitor both the horizontal and vertical movement of the rotor simultaneously. The movement of the rotor is displaced as a circle on the computer. The piezoelectric accelerometers employed are constant current

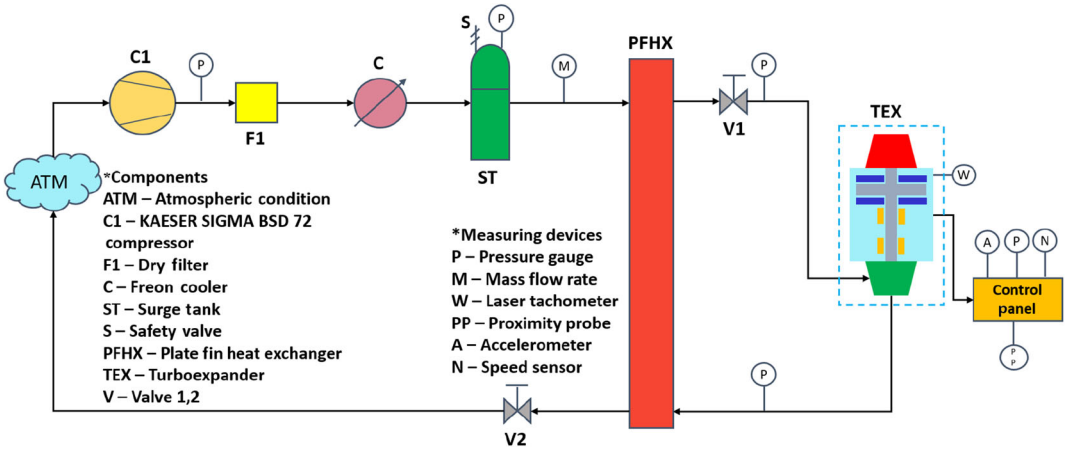

Figure 4. Schematic diagram of the test setup.

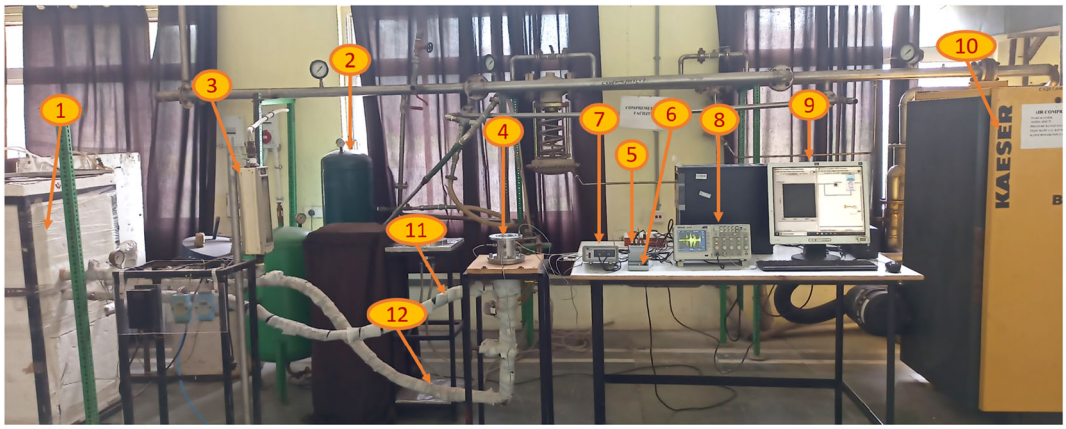

1. PFHX, 2. Reservoir, 3. Rotameter, 4. Turboexpander, 5. NI cDAQ-9185, 6. NI 9234 vibration card, 7. Demodulator, 8. Oscilloscope, 9. , 10. KAESER SIGMA BSD72 compressor, 11. Turbine inlet, 12. Turbine outlet

Figure 5. Experimental test rig.

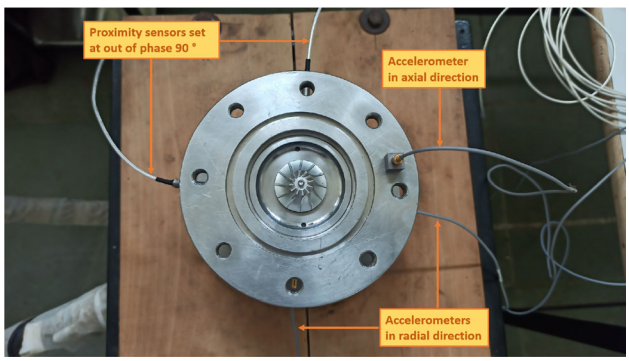

Figure 6. Arrangement plan for vibration signals.

Table 4. Specifications of the sensors.

Probe	Make	Model	Type	Sensitivity	Range
Prox1	Spectraquest	035210	Inductive	4.52 V/mm	0–5 kHz
Prox2	Spectraquest	035210	Inductive	4.39 V/mm	0–5 kHz
Acc1	B & K	4508	IEPE	9.841 mV/m/s^2	0–8 kHz
Acc2	B & K	4508	IEPE	9.841 mV/m/s^2	0–8 kHz
Acc3	B & K	4508	IEPE	9.841 mV/m/s^2	0–8 kHz

line drive (CCLD) devices with built-in low-noise pre-amplifiers that are suited for multi-channel modal analysis experiments. Three uniaxial accelerometers are installed on the bearing housing using white bee wax in radial and axial directions. The accelerometer is a device that translates vibrational acceleration into an electric output. The output of the accelerometer signal is recorded in an oscilloscope through a cable.

Figure 6 illustrates the offset of the two proximity probes in the rotor radial direction at the bearing location and three accelerometers, one in axial and two in radial directions. The specifications of the proximity sensors and the accelerometers are given in table 4.

3. Finite element modelling of the high-speed rotor

The rotor is made up of a steel shaft, a collar, a turbine, a compressor and two journal bearings, as given in figure 7. A total of 90 Timoshenko beam finite elements have been used to discretize the rotor, each with its own fundamental matrix and suitable disc finite elements for the discs. The full system model has 364 DOFs. Two journal foil bearings are used to support the rotor (nodes 27 and 61), with a maximum radial clearance of 60 μm. The turbine and compressor are located at the two ends. The residual unbalance, after balancing, is less than 40 mg-mm measured at the planes of the bearings.

3.1 *Motion equation of the rotor*

The shaft is modelled by using the Timoshenko beam theory. The rotary and translatory inertia, shear deformation and gyroscopic moments are considered in the system. Each element of the rotor has two nodes and each node has four DOFs (two translational in x and y direction and two rotational around x and y axis). Thus, the DOFs for a shaft element are demonstrated as $\{q_e\} = \{u_1 \quad v_1 \quad \xi_1 \quad \psi_1 \quad u_2 \quad v_2 \quad \xi_2 \quad \psi_2\}^T$. The compressor, collar, and turbine are represented as discs with lumped mass and inertia. These are incorporated in the global mass and gyroscopic matrix at the appropriate node. The dynamic expression of the shaft elements [26] is given as follows.

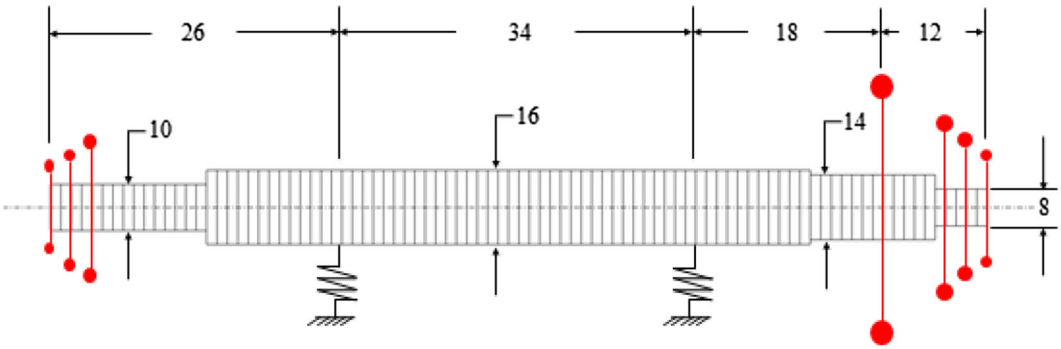

Figure 7. FE model of the turboexpander rotor.

$$[[M_e^T]_S + [M_e^R]_S]\{\ddot{q}_e\} - \omega[G_e]_S\{\dot{q}_e\} + [K_e]_S\{q_e\} = \{F_e\}_S \quad (1)$$

where M, G, K and F represent the mass, gyroscopic, stiffness and force components respectively, the super-indexes T and R denote the translatory and rotary components respectively, and sub-indexes e and S stand for the element and shaft respectively. The symbols and notations are given in the Nomenclature, and the detailed derivation of the equations is given in the Appendix.

3.2 *Motion equation of the disc*

The dynamic expression of the rigid disk [26] is demonstrated as

$$[M_e]_D\{\ddot{q}_e\} - \omega[G_e]_D\{\dot{q}_e\} = \{F_e\}_D \quad (2)$$

Where the sub-index D stands for the disc.

3.3 *Motion equation of the gas foil bearings*

The bearings are integrated into the model by taking into account their stiffness and damping characteristics. The dynamic equation of bearing [26] is formulated as

$$[C]_B\{\dot{q}_e\} + [K]_B\{q_e\} = \{F_e\}_B \quad (3)$$

Where C represents the damping and the sub-index B stands for the bearing.

The authors have previously calculated the dynamic coefficients of the gas foil bearing [27]. The change in stiffness and damping coefficients with respect to speed have been used in this study.

3.4 *Global motion equation of the high-speed rotor system*

The rotor-disk-bearing model's dynamic equation of motion can be stated in a global form [26] as

$$[M]\{\ddot{q}\} + [C]\{\dot{q}\} + [K]\{q\} = \{F\} \quad (4)$$

Where global mass matrix $[M] = [M_e^T]_s + [M_e^R]_s + [M_e]_D$, global stiffness matrix $[K] = [K_e]_s + [K]_B$, global damping matrix $[C] = [C]_B - \omega[G_e]_s - \omega[G_e]_D$ and global force vector $\{F\} = \{F_e\}_s + \{F_e\}_D + \{F_e\}_B$ respectively.

4. Model validation

Before conducting the FE analysis of the turboexpander, it is important to access the verification of the model. The obtained response from the present model is compared to the FE model [28], as shown in figure 8. The comparison reveals a good agreement between both the models and validates the accuracy of the present model.

5. Numerical results and discussion

The FE analysis of the turboexpander is conducted before the experimental investigation to predict the dynamic behavior of the rotor.

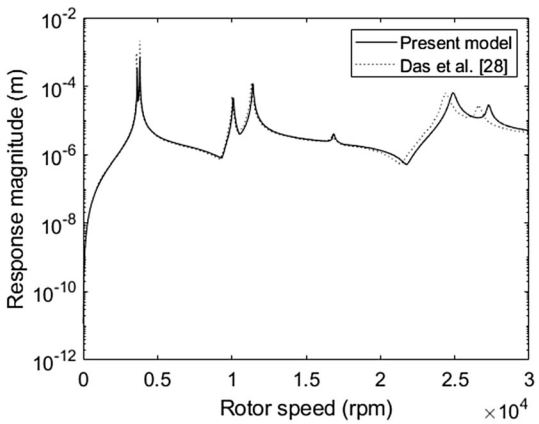

Figure 8. Comparison of unbalance response between the present model and Das *et al* [28].

5.1 *Campbell diagram and unbalance response*

The critical speed of the turboexpander rotor system is estimated from the Campbell diagram, as shown in figure 9. The line (dashed) with a 45° inclination is the synchronous whirl line, which represents the excitation spin speed. The critical speed is the point where the whirling line and synchronous whirl line intersect.

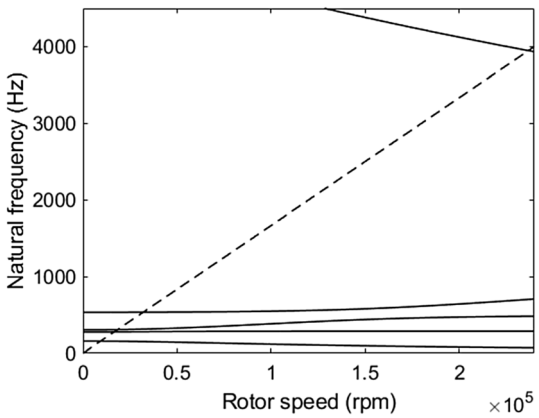

Figure 9. Campbell diagram.

Because the high-order natural frequencies exceed the operational speed, only the first two order natural frequencies are shown. For each order natural frequency, there exists the forward and backward whirling frequency. The first two forward critical speeds occur at 16579.56 and 32031.00 rpm, respectively, while the corresponding backward critical speeds are 9371.90 and 18403.56 rpm.

Figure 10 shows the unbalance response of the rotor evaluated at nodes 1, 27, 61 and 91 respectively. The peaks were found at 9371.91 rpm, 16579.96 rpm, 18403.56 rpm and 32031 rpm and 231,892.56 rpm respectively. These are identified as the critical speeds of the rotor. The vibration near the journal bearings is found to be highest at the 4th critical speed (32,031 rpm). The maximum vibration amplitude is 52.32 μm at the first bearing and 53.41 μm at the second bearing. The highest response at the turbine and compressor end is observed to be 54.2 μm and 18.15 μm respectively. The maximum vibration which occurs at the turbine end is close to the 4th critical speed. The turbomachinery must be operated far from this critical speed in order to avoid failure of the rotor. However, the bending critical speed is observed to be 231,892.56 rpm. It was decided to operate within the 4th and 5th critical speed far from all the peaks. The experiments are conducted at the

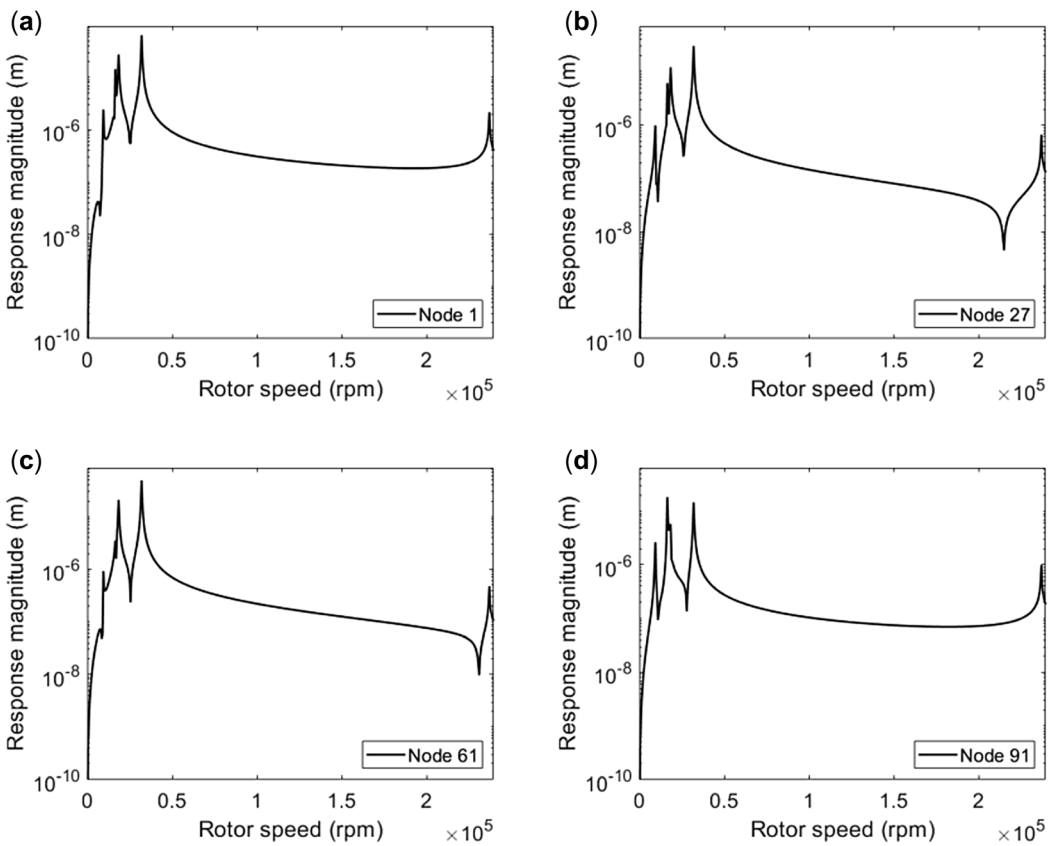

Figure 10. Unbalance response at (**a**) turbine end, (**b**) bearing near the turbine, (**c**) bearing near the compressor and (**d**) compressor end.

design speed of 175,000 rpm for the safe operation of the rotor.

5.2 *Mode shapes and orbits*

The first six mode shapes of the turboexpander rotor system are shown in figure 11. It is observed that the shapes for forward and backward modes are identical for the same order mode. The first and second order mode shapes of the rotor are both rigid body modes, whereas the third order mode shape is bending mode. The first order mode shape is the translatory whirl and the second order mode shape is the conical whirl. The backward and forward whirl of the first order mode shape corresponds to a rotational speed of 156.88 Hz and 274.91 Hz respectively. The corresponding second-order mode shapes are 304.05 Hz and 532.67 Hz respectively. These critical speeds are far lower than the designed rotor speed of 175,000 rpm. Catastrophic transverse vibrations may occur if the rotation speed comes near these critical speeds. Therefore, preventive action must be taken during the turboexpander testing phase so as to quickly surpass the critical speeds. The mode shape associated with the third order mode resembles a half sine wave. This critical speed is the bending critical speed, and it is vital for the design of the high-speed rotor. The turboexpander must be operated far from this critical speed in order to avoid failure of the rotor.

It is important to identify the direction of the forward and backward whirling components. The orbit of any point on the shaft is now elliptical rather than circular. This is illustrated in figure 12, which shows an axial view of the

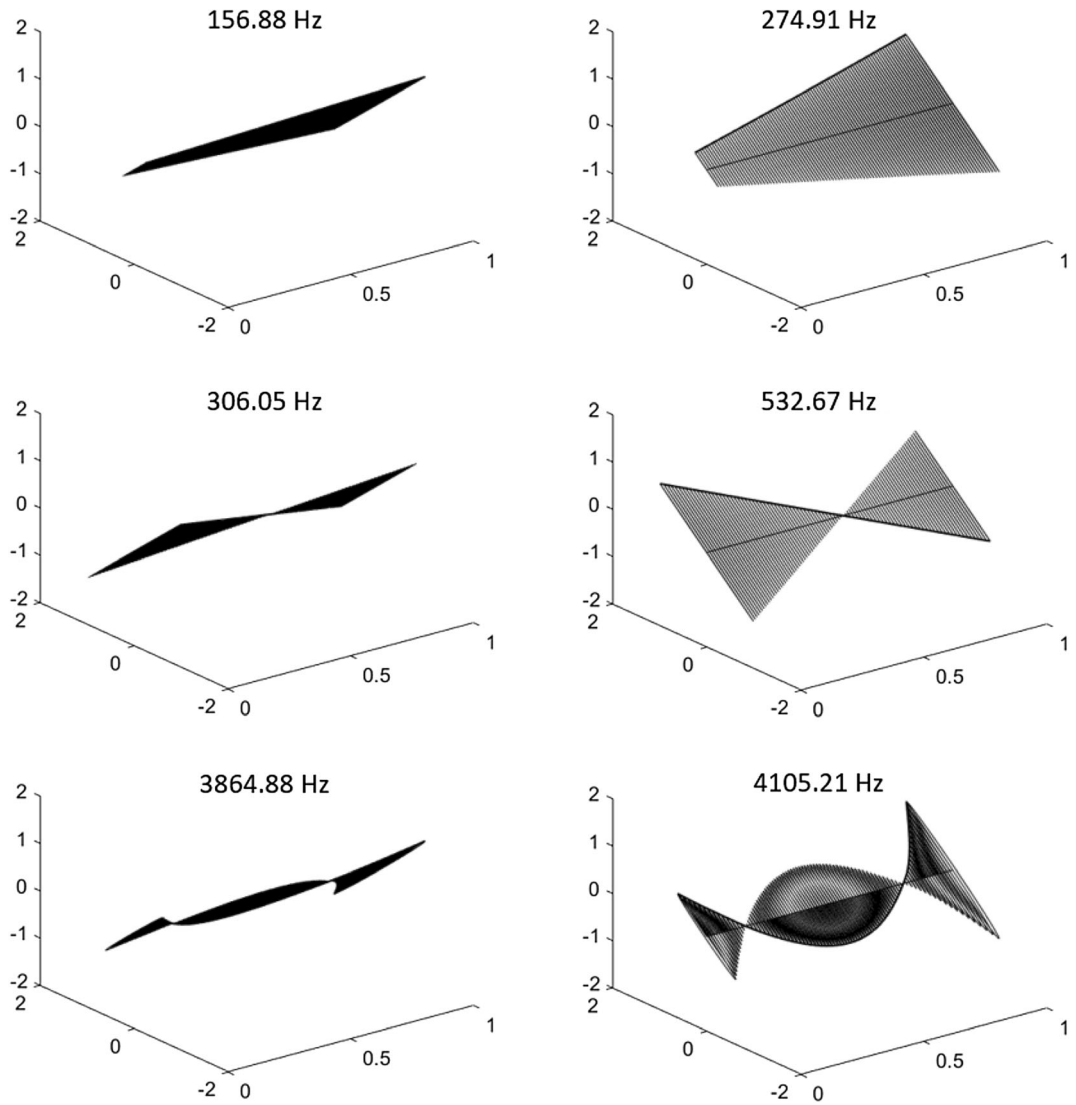

Figure 11. Mode shapes of the turboexpander rotor.

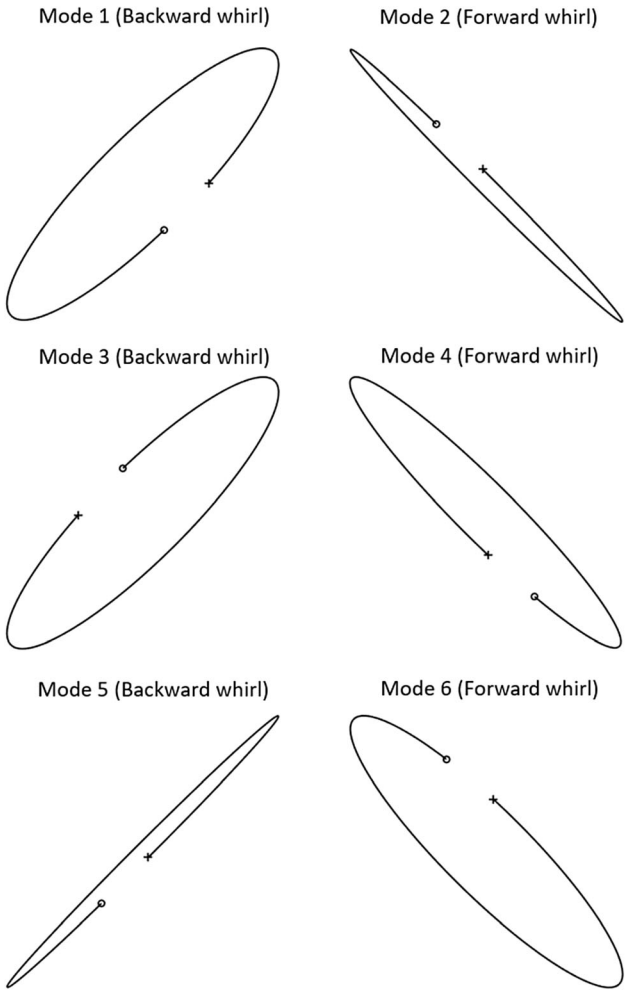

Figure 12. The axial view of mode shapes (the circle denotes the start of the orbit and the plus denotes the end).

mode shapes. The orbits indicate that the odd-numbered modes are backward at all nodes, whereas the even-numbered modes precess forward at all nodes.

6. Experimentation and correlation with numerical results

The vibration is measured at various locations and analyzed by using the NI multi-channel data acquisition system along with the NI LabVIEW software. After mounting the probes and connecting all the devices, the pressure valve was gradually opened to enable the air to hit the turbine and the rotor to start running. After the rotor started running at a constant stable speed, the valve was gradually fully opened, permitting the rotor to operate at full speed of 175,000 rpm. Due to certain limitations of the compressor available in the laboratory, the speed was limited to a certain extent.

6.1 *Mass unbalance response*

The bearings, turbine and compressor sides maintain a very low clearance during operation. Therefore, the high amplitude of vibrations at these locations prevents the smooth operation of the turbomachinery. Figure 13 compares the unbalanced mass response obtained from the experiments and the FE analysis at bearing locations. The same set of experiments was conducted three times to ensure sufficient repeatability. It was observed that there was a marginal deviation between the set of experiments. The standard deviation was calculated to evaluate the error between the data sets. The error bars represent the error from the experimental data. The findings of the mass imbalance response analysis depict that the predictions agree well with the measured experimental results. A marginal relative error of 2–9 % is found at the journal

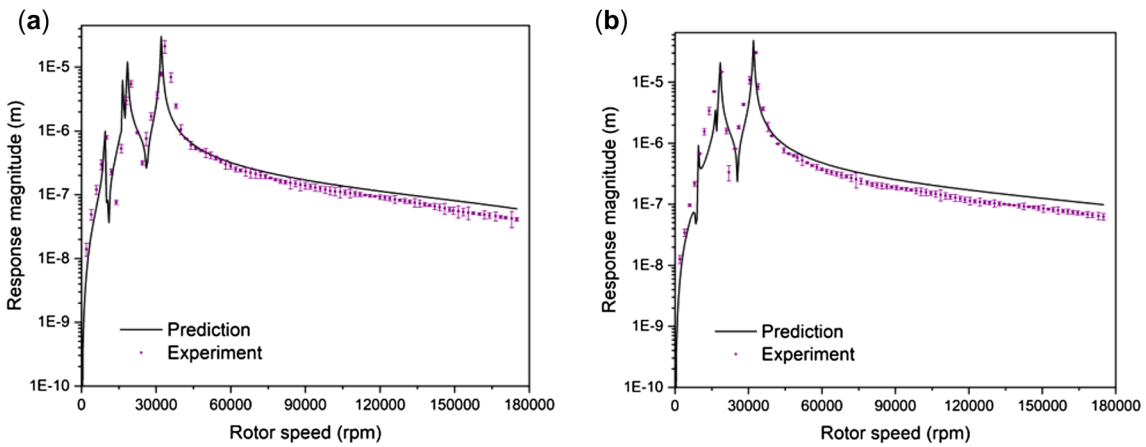

Figure 13. Comparison of predicted and measured unbalance response at (**a**) journal bearing near the turbine, (**b**) journal bearing near the compressor.

Table 5. Comparison between experimental and analysis results for critical speeds of the rotor.

Order	Experiment (rpm)	Analysis (rpm)	Relative error (%)
1st	9761	9371	3.9
2nd	17,304	16,579	4.1
3rd	19,307	18,403	4.6
4th	34,137	32,031	6.1

bearing locations. It was observed that the response amplitude increased near the critical speeds owing to the resonance.

With the increment of rotating speed, the response amplitude increased gradually, and a number of peaks were found around 9761 rpm, 17,304 rpm, 19,307 rpm and 34,137 rpm. These speeds were identified as the critical speeds of the turbomachinery. The highest peak among these was found to be about 50 μm at the speed of nearly 34,000 rpm. The amplitude value is lower than the 60 μm designed radial clearance of the bearings, which depicts the safe design of the journal. It is observed that the response amplitude peaks under the critical speed at both the bearing locations are marginally different. This is because the rotor is longitudinally not symmetrical and the disc is present at an offset position on the rotor.

From the FE analysis, the first four critical speeds were found to be around 9371 rpm, 16,579 rpm, 18,403 rpm and 32,031 rpm respectively. Table 5 presents the relative error for the first-order to fourth-order natural frequencies generated from the experiment and prediction. The findings show an error of 3-6 %, suggesting that the experiment and prediction were credible. This marginal error is primarily due to the dimensional tolerance during fabrication. There may also be a time delay in the experimental critical speed because of the relatively high speed-up rate. The highest peak at the journal bearing near the turbine and compressor side is observed to be 52.32 μm and 53.41 μm respectively. The maximum response occurs at the journal bearing near the turbine at the speed of 32,030 rpm and this speed is near the computed fourth critical speed of the rotor.

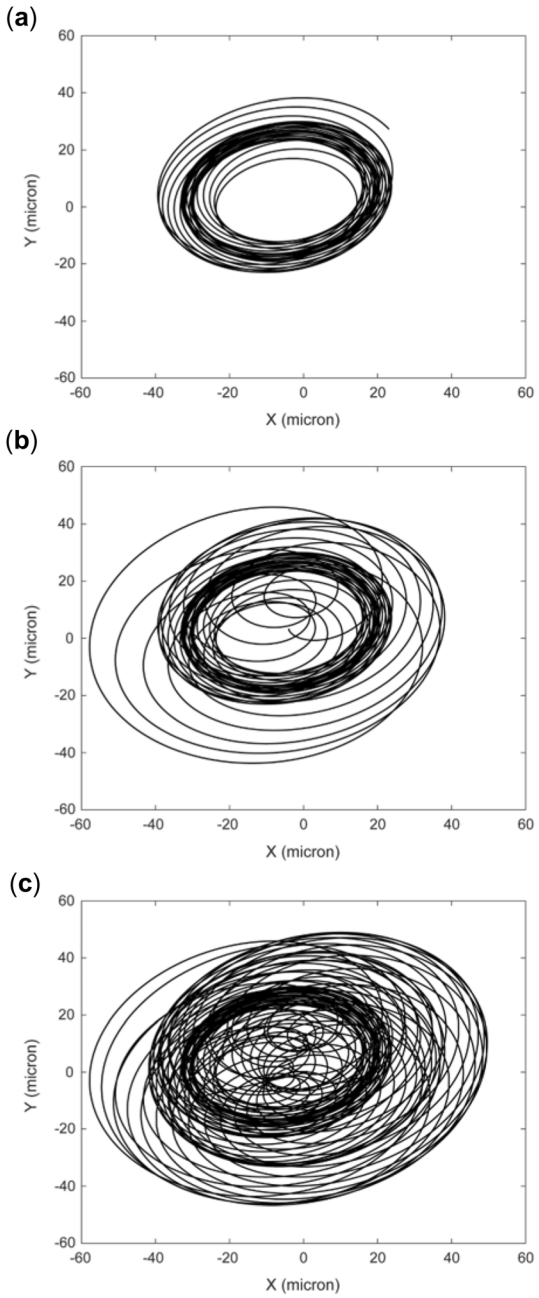

Figure 14. Shaft trajectory at (**a**) 10,000 rpm, (**b**) 20,000 rpm and (**c**) 30,000 rpm.

6.2 *Rotor orbits*

The data from the waveforms of the two proximity sensors that are out of phase 90° are combined to generate a graph that shows the movement of the shaft center in two dimensions. Rotor trajectories at three rotational speeds, 10,000 rpm and 20,000 rpm and 30,000 rpm, are shown in figure 14a, b and c respectively.

The orbits are found to share nearly a similar pattern of vibration and the rotor trajectory is observed to be stable at first. Then, the trajectory tends to become distorted as the speed increases and forms an elliptical path around the center position. A significant increase in the amplitude of overall rotor motions is observed with the increase in rotor speed. The total precession magnitudes are found to be within − 60 μm to 60 μm in both the x direction and y direction. It is difficult to identify the direction of rotation of the rotor from the orbit experimentally. Examining the machine is the best technique to establish the rotational direction. Another approach is to observe rotating orbits in slow motion that act in the direction of the precession movement.

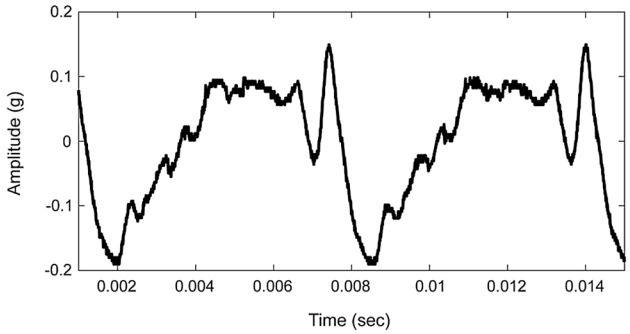

Figure 15. Spectrum in time domain close to 1st rigid critical speed (9761 rpm) near journal bearing of turbine side.

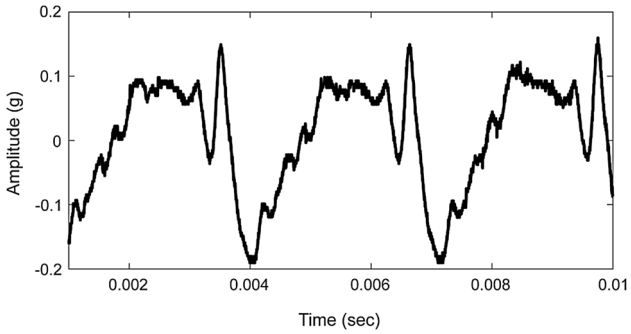

Figure 17. Spectrum in time domain close to 3rd rigid critical speed (19,307 rpm) near journal bearing of turbine side.

6.3 *Transient rotor vibrations*

Accelerometers are used as measurement tools for accurately sensing the vibration of bearing housings and cases. The signal from the accelerometer is recorded on a storage type oscilloscope during test runs. The oscilloscope shows the vibration level of the housing close to the bearing locations. During the phase of increasing speed, four critical speeds are noticed where the vibration level is suddenly increased. Transient vibrations of the rotor at these critical speeds are recorded and shown in figures 15, 16, 17 and 18.

The first critical speed is around 9761 rpm at 0.2 MPa, the second is around 17,304 rpm at 0.25 MPa supply, the third is around 19,307 rpm at 0.34 MPa and the fourth is around 34,137 at 0.46 MPa of inlet pressure to the turbine. These speeds are close to the predicted critical speeds of the rotor, as described in section 6.1. The marginal deviation in critical speed is a testament to the accuracy of the rotodynamic predictions. The critical speeds are noted, and in the successive runs, these speeds are quickly crossed to avoid any excessive vibration of the turboexpander.

6.4 *Fast Fourier transform of the transient signals*

The rotor was able to achieve a stable rotating speed of close to 1,75,000 rpm with a supply pressure of 0.8 MPa. The fast Fourier transform (FFT) of the transient signals near the journal bearing of turbine side and compressor side at 1,75,000 rpm is shown in figures 19 and 20 respectively. Similarly, the FFT near the turbine end and compressor end is shown in figures 21 and 22 respectively. Three sets of experiments are conducted to ensure sufficient repeatability. The error bars in figures 19, 20, 21 and 22 show the error from the experimental data.

The synchronous vibration amplitude was found to be around 56 μm found near the journal bearing of turbine side. A pick is observed close to the 2× speed (5950 Hz), which may be caused by mechanical looseness and misalignment of the bearing unit. A subharmonic frequency is found near 0.5× (1498 Hz). The subharmonic frequency occurs may be due to the whirling of the rotor. The rotor whirling is a self-excited instability generated by gas whirling in the bearing clearance. A marginal difference in the level of vibration near the upper and lower journal bearing is observed owing to rotor whirling and misalignment. The vibration at the turbine end is found to be higher than that of the compressor end due to the presence of air supply ports.

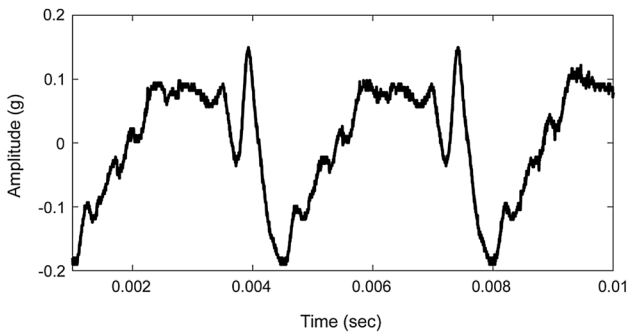

Figure 16. Spectrum in time domain close to 2nd rigid critical speed (17,304 rpm) near journal bearing of turbine side.

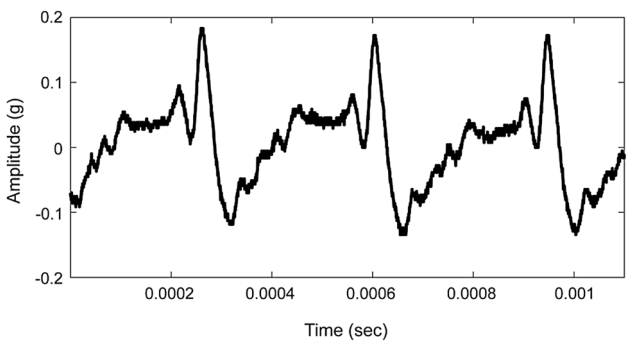

Figure 18. Spectrum in time domain close to 4th critical speed (34,137 rpm) near journal bearing of turbine side.

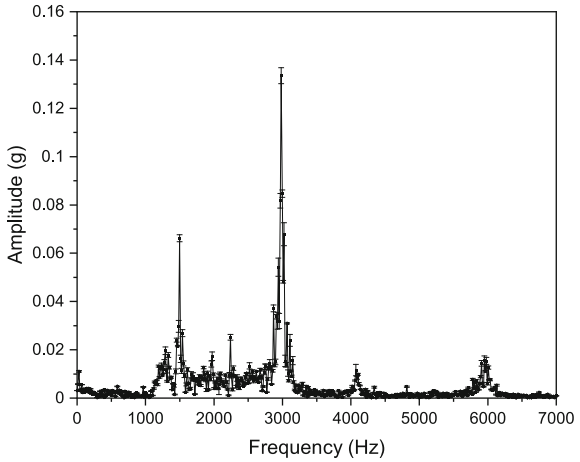

Figure 19. FFT at speed of 1,75,000 rpm near journal bearing of turbine side.

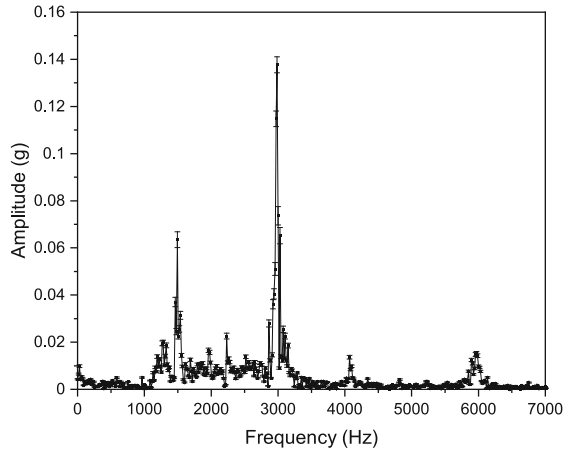

Figure 20. FFT at speed of 1,75,000 rpm near journal bearing of compressor side.

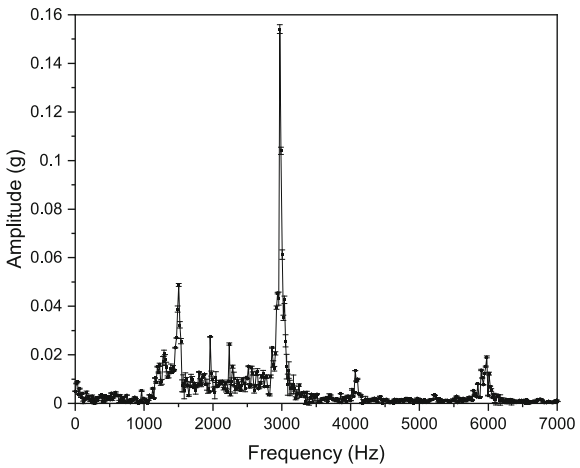

Figure 21. FFT at speed of 1,75,000 rpm near turbine end.

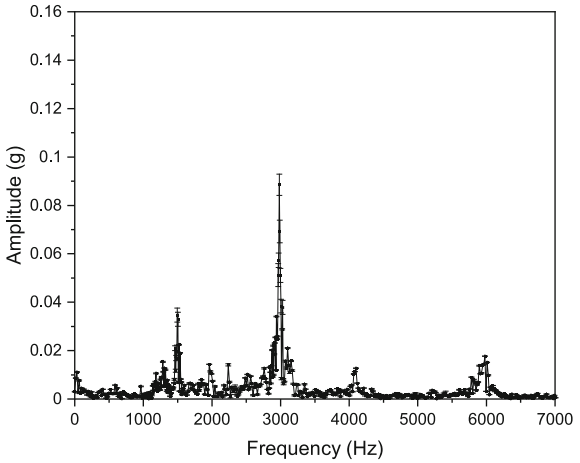

Figure 22. FFT at speed of 1,75,000 rpm near compressor end.

7. Conclusions

Based on the research conducted on the rotordynamic performance of the turboexpander rotor supported on gas foil bearings, the following conclusions have been drawn:

1. The Campbell diagram showed only the first two order natural frequencies as the high-order natural frequencies exceeded the operational speed. The unbalance response depicts that the highest response is 54.2 μm and 18.15 μm at the turbine and compressor end respectively.
2. The shapes for forward and backward modes are observed to be identical for the same order mode. The first and second order mode shapes of the rotor are rigid body modes, whereas the third order mode shape is the bending mode. The axial view of the mode shapes is observed to identify the direction and shape of the forward and backward whirling components. It is found that the odd-numbered modes are backward at all nodes, whereas the even-numbered modes precess forward at all nodes.
3. The trend of the mass unbalance response from the experiments was found to be similar to that of the finite element analysis, which confirms the reliability of the experiments. The response amplitude was observed to increase near the critical speeds owing to the resonance. A marginal relative error of $3-6\%$ was found upon the comparison of experimental natural frequencies with the predictions.
4. The rotor orbit trajectory is found to form an elliptical path around the center position. A significant increase in the amplitude of rotor motions is observed with the increase in rotor speed. Vibrations of the rotor at the critical speeds are recorded, and the total precession magnitudes are found to be within the range of $-$ 60 μm to 60 μm in both the x direction and y direction.

5. The synchronous vibration amplitude is recorded, and the occurrence of subharmonic frequency components at the bearing locations is addressed. A marginal difference in the level of vibration near the upper and lower journal bearing is observed owing to rotor whirling and misalignment. The vibration at the turbine end is found to be higher than that of the compressor end due to the presence of air supply ports.

Appendix

A.1. Shaft element matrices

$$[M_e^T]_s = \frac{\rho A L_e}{840(1+\Phi)^2}\begin{bmatrix} m_1 & 0 & 0 & m_2 & m_3 & 0 & 0 & m_4 \\ 0 & m_1 & -m_2 & 0 & 0 & m_3 & -m_4 & 0 \\ 0 & -m_2 & m_5 & 0 & 0 & m_4 & m_6 & 0 \\ m_2 & 0 & 0 & m_5 & -m_4 & 0 & 0 & m_6 \\ m_3 & 0 & 0 & -m_4 & m_1 & 0 & 0 & -m_2 \\ 0 & m_3 & m_4 & 0 & 0 & m_1 & m_2 & 0 \\ 0 & -m_4 & m_6 & 0 & 0 & m_2 & m_5 & 0 \\ m_4 & 0 & 0 & m_6 & -m_2 & 0 & 0 & m_5 \end{bmatrix} \tag{A.1}$$

$$[M_e^R]_s = \frac{\rho \mathrm{I}}{30L_e(1+\Phi)^2}\begin{bmatrix} m_7 & 0 & 0 & m_8 & -m_7 & 0 & 0 & m_8 \\ 0 & m_7 & -m_8 & 0 & 0 & m_7 & -m_8 & 0 \\ 0 & -m_8 & m_9 & 0 & 0 & m_8 & m_{10} & 0 \\ m_8 & 0 & 0 & m_9 & -m_8 & 0 & 0 & m_{10} \\ -m_7 & 0 & 0 & -m_8 & m_7 & 0 & 0 & -m_8 \\ 0 & -m_7 & m_8 & 0 & 0 & m_7 & m_8 & 0 \\ 0 & -m_8 & m_{10} & 0 & 0 & m_8 & m_9 & 0 \\ m_8 & 0 & 0 & m_{10} & -m_8 & 0 & 0 & m_9 \end{bmatrix} \tag{A.2}$$

$$[G_e]_s = \frac{\rho \mathrm{I}}{15L_e(1+\Phi)^2}\begin{bmatrix} 0 & -g_1 & g_2 & 0 & 0 & g_1 & g_2 & 0 \\ g_1 & 0 & 0 & g_2 & -g_1 & 0 & 0 & g_2 \\ -g_2 & 0 & 0 & -g_3 & g_2 & 0 & 0 & -g_4 \\ 0 & -g_2 & g_3 & 0 & 0 & g_2 & g_4 & 0 \\ 0 & g1 & -g_2 & 0 & 0 & -g_1 & -g_2 & 0 \\ -g_1 & 0 & 0 & -g_2 & g_1 & 0 & 0 & -g_2 \\ -g_2 & 0 & 0 & -g_4 & g_2 & 0 & 0 & -g_3 \\ 0 & -g_2 & g_4 & 0 & 0 & g_2 & g_3 & 0 \end{bmatrix} \tag{A.3}$$

$$[K_e]_s = \frac{\mathrm{EI}}{L_e^3(1+\Phi)}\begin{bmatrix} 12 & 0 & 0 & 6L_e & -12 & 0 & 0 & 6L_e \\ 0 & 12 & -6L_e & 0 & 0 & -12 & -6L_e & 0 \\ 0 & -6L_e & (4+\Phi)L_e^2 & 0 & 0 & 6L_e & (2-\Phi)L_e^2 & 0 \\ 6L_e & 0 & 0 & (4+\Phi)L_e^2 & -6L_e & 0 & 0 & (2-\Phi)L_e^2 \\ -12 & 0 & 0 & -6L_e & 12 & 0 & 0 & -6L_e \\ 0 & -12 & 6L_e & 0 & 0 & 12 & 6L_e & 0 \\ 0 & -6L_e & (2-\Phi)L_e^2 & 0 & 0 & 6L_e & (4+\Phi)L_e^2 & 0 \\ 6L_e & 0 & 0 & (2-\Phi)L_e^2 & -6L_e & 0 & 0 & (4+\Phi)L_e^2 \end{bmatrix} \tag{A.4}$$

Where,

$$
\begin{aligned}
m_1 &= 312 + 588\Phi + 280\Phi^2,\\
m_2 &= (44 + 77\Phi + 35\Phi^2)L_e,\\
m_3 &= 108 + 252\Phi + 140\Phi^2,\\
m_4 &= -(26 + 63\Phi + 35\Phi^2)L_e,\\
m_5 &= (8 + 14\Phi + 7\Phi^2)L_e^2,\\
m_6 &= -(6 + 14\Phi + 7\Phi^2)L_e^2,\\
m_7 &= 36,\\
m_8 &= (3 - 15\Phi)L_e,\\
m_9 &= (4 + 5\Phi + 10\Phi^2)L_e^2,\\
m_{10} &= (-1 - 5\Phi + 5\Phi^2)L_e^2,\\
g_1 &= 36,\\
g_2 &= (3 - 15\Phi)L_e,\\
g_3 &= (4 + 5\Phi + 10\Phi^2)L_e^2,\\
g_4 &= (-1 - 5\Phi + 5\Phi^2)L_e^2.
\end{aligned}
$$

A.2. Bearing matrices

$$
[C]_B = \begin{bmatrix} C_{xx} & C_{xy} \\ C_{yx} & C_{YY} \end{bmatrix} \quad [K]_B = \begin{bmatrix} K_{xx} & K_{xy} \\ K_{yx} & K_{YY} \end{bmatrix} \qquad (A.5-6)
$$

A.3. Disc matrices

$$
\begin{aligned}
[M_e]_D &= \begin{bmatrix} m_d & 0 & 0 & 0 \\ 0 & m_d & 0 & 0 \\ 0 & 0 & I_d & 0 \\ 0 & 0 & 0 & I_d \end{bmatrix} \quad [G_e]_D \\
&= \begin{bmatrix} 0 & 0 & 0 & 0 \\ 0 & 0 & 0 & 0 \\ 0 & 0 & 0 & -I_p \\ 0 & 0 & I_p & 0 \end{bmatrix} \qquad (A.7-8)
\end{aligned}
$$

List of symbols

$[M_e^T]_S$	Translatory mass matrix of the shaft
$[M_e^R]_S$	Rotary mass matrix of the shaft
$[G_e]_S$	Gyroscopic matrix of the shaft
$[K_e]_S$	Stiffness matrix of the shaft
$\{F_e\}_S$	Generalized force vector of the shaft element
$[M_e]_D$	Mass matrix of the disc
$[G_e]_D$	Gyroscopic matrix of the disc
$\{F_e\}_D$	Generalized force vector of the disk element
q	Displacement vector
u	Displacement of node in X direction
v	Displacement of node in X direction
$[C]_B$	Damping matrix of the bearing
$[K]_B$	Stiffness matrix of the bearing
$\{F_e\}_B$	Generalized force vector of the bearing
$[M]$	Global mass matrix
$[C]$	Global damping matrix
$[K]$	Global stiffness matrix
$\{F\}$	Global force vector
ω	Angular velocity
ξ	Rotational displacement of node about X direction
ψ	Rotational displacement of node about Y direction

Declarations

Conflict of interest The authors declared that there is no conflict of interest to any person or organization.

References

[1] DellaCorte C, Zaldana A R and Radil K C 2004 A systems approach to the solid lubrication of foil air bearings for oil-free turbomachinery. *J. Trib.* 126: 200–207

[2] Waumans T, Peirs J, Al-Bender F and Reynaerts D 2011 Aerodynamic journal bearing with a flexible, damped support operating at 7.2 million DN. *J. Micromech. Microeng.* 21: 104014

[3] Pattnayak M R, Dutt J K and Pandey R K 2022 Rotordynamics of an accelerating rotor supported on aerodynamic journal bearings. *Tribol. Int.* 176: 107883

[4] Li L, Zhang D and Xie Y 2019 Effect of misalignment on the dynamic characteristic of MEMS gas bearing considering rarefaction effect. *Tribol. Int.* 139: 22–35

[5] Yang Q, Liu Y and Zhang H 2016 Unbalance response of micro gas bearing-rotor system considering rarefaction effect. *Proc. Inst. Mech. Eng. Part J J. Eng. Tribol.* 230: 281–288

[6] Zhang W M, Meng G and Wei K X 2012 Numerical prediction of surface roughness effect on slip flow in gas-lubricated journal microbearings. *Tribol. Trans.* 55: 71–76

[7] Pattnayak M R, Pandey R K and Dutt J K 2020 Performance behaviours of a self-acting gas journal bearing with a new bore design. *Tribol. Int.* 151: 106418

[8] Pattnayak M R, Pandey R K and Dutt J K 2021 Effects of new micro-pocketed bore surface topographies on the performance behaviours of aerodynamic journal bearing. *Surf. Topogr. Metrol. Prop.* 9: 025001

[9] Liu W, Bättig P, Wagner P H and Schiffmann J 2021 Nonlinear study on a rigid rotor supported by herringbone grooved gas bearings: Theory and validation. *Mech. Syst. Signal Process.* 146: 106983

[10] Miyanaga N and Tomioka J 2015 Stability analysis of Herringbone-grooved aerodynamic journal bearings for ultra high-speed rotations. *Int. J. Mater. Mech. Manuf.* 4: 156–161

[11] Schiffmann J 2013 Enhanced groove geometry for herringbone grooved journal bearings. *J. Eng. Gas Turbines Power.* 135: 102501

[12] Schiffmann J and Favrat D 2010 Integrated design and optimization of gas bearing supported rotors. *J. Mech. Des.* 132: 051007

[13] Pattnayak M R, Ganai P, Pandey R K, Dutt J K and Fillon M 2022 An overview and assessment on aerodynamic journal

bearings with important findings and scope for explorations. *Tribol. Int.* 174: 107778

[14] Hayashi K and Hirasata K 1995 Developments of aerodynamic foil bearings for small high-speed rotor. *Tribol. Ser.* 30: 291–299

[15] Walton J F and Heshmat H 1994 Compliant foil bearings for use in cryogenic turbopumps. *NASA CP* 3282(1): 372–381

[16] Xiong L Y, Wu G, Hou Y, Liu L Q, Ling M F and Chen C Z 1997 Development of aerodynamic foil journal bearings for a high speed cryogenic turboexpander. *Cryogenics.* 37: 221–230

[17] Hou Y, Xiong L Y, Wang J, Lin M F and Chen C Z 2000 The experimental study of aerodynamic plate-foil journal bearings for High Speed Cryogenic Turboexpander. *Tribol. Trans.* 43: 681–684

[18] Walton J F and Hesmat H 2002 Application of foil bearings to turbomachinery including vertical operation. *J. Eng. Gas Turbines Power.* 124: 1032–1041

[19] Hou Y, Zhu Z H and Chen C Z 2004 Comparative test on two kinds of new compliant foil bearing for small cryogenic turbo-expander. *Cryogenics.* 44: 69–72

[20] Lai T, Chen S, Ma B, Zheng Y and Hou Y 2014 Effects of bearing clearance and supporting stiffness on performances of rotor-bearing system with multi-decked protuberant gas foil journal bearing. *Proc. Inst. Mech. Eng. Part J J. Eng. Tribol.* 228: 780–788

[21] Lai T, Guo Y, Zhao Q, Wang Y, Zhang X and Hou Y 2018 Numerical and experimental studies on stability of cryogenic turbo-expander with protuberant foil gas bearings. *Cryogenics.* 96: 62–74

[22] Özşahin O, Özgüven H N and Budak E 2014 Analytical modeling of asymmetric multi-segment rotor-bearing systems with Timoshenko beam model including gyroscopic moments. *Comput. Struct.* 144: 119–126

[23] Nikolajsen J L 2001 Finite element and transfer matrix methods for rotordynamics: A comparison. In: *ASME Turbo Expo: Power for Land, Sea, and Air,* pp. V004T03A002

[24] Jalali M H, Ghayour M, Ziaei-Rad S and Shahriari B 2014 Dynamic analysis of a high speed rotor-bearing system. *Measurement.* 53: 1–9

[25] Han D, Bi C and Yang J 2019 Nonlinear dynamic behavior research on high-speed turbo-expander refrigerator rotor. *Eng. Fail. Anal.* 96: 484–495

[26] Friswell M I 2010 Dynamics of Rotating Machines. Cambridge University Press, New York

[27] Khamari D S, Kumar J and Behera S K 2021 Numerical investigation of influence sensitivity of a gas foil bearing parameters on the dynamic coefficients. *J. Braz. Soc. Mech. Sci. Eng.* 43: 1–19

[28] Das A S and Dutt J K 2008 Reduced model of a rotor-shaft system using modified SEREP. *Mech. Res. Commun.* 35: 398–407